Acta Materialia 284 (2025) 120585

Contents lists available at ScienceDirect

Acta Materialia

journal homepage: www.elsevier.com/locate/actamat

Physicochemical properties of $La_{0.5}Ba_{0.5}Co_{1-x}Fe_xO_{3-\delta}$ ($0 \leq x \leq 1$) as positrode for proton ceramic electrochemical cells

Sebastian L Wachowski [a,*], Iga Szpunar [a], Joanna Pośpiech [a], Daria Balcerzak [a], Aleksandra Mielewczyk-Gryń [a], Małgorzata Nadolska [a], María Balaguer [b], José M. Serra [b], Einar Vøllestad [c], Maria Gazda [a], Ragnar Strandbakke [c,d], Truls Norby [d]

[a] *Faculty of Applied Physics and Mathematics, Institute of Nanotechnology and Materials Engineering, Gdańsk University of Technology, ul. G. Narutowicza 11/12, Gdańsk 80-233, Poland*
[b] *Instituto de Tecnología Química, Universitat Politècnica de València - Consejo Superior de Investigaciones Científicas, Avenida de los Naranjos s/n, Valencia 46022, Spain*
[c] *SINTEF Industry, Sustainable Energy Technology, POB 124 Blindern, NO-0314 Oslo, Norway*
[d] *Department of Chemistry, Centre for Materials Science and Nanotechnology, University of Oslo, Gaustadalléen 21, NO-0349 Oslo, Norway*

ARTICLE INFO

Keywords:
Mixed conductor
Conductivity
X-ray synchrotron radiation
Polaron
p-type
Hydration

ABSTRACT

We report on essential properties of materials in the series $La_{0.5}Ba_{0.5}Co_{1-x}Fe_xO_{3-\delta}$ as positrodes for proton ceramic electrochemical cells (PCECs). The unit cell and thermochemical expansion coefficient (TCEC) of these cubic perovskites decrease with iron content x, the TCEC of $La_{0.5}Ba_{0.5}FeO_{3-\delta}$ going as low as $11\cdot10^{-6}$ 1/K. The materials behave as $LaMO_3$ perovskites with small band gaps and Ba acting as acceptors compensated by electron holes and oxygen vacancies. The electrical properties are dominated by p-type conduction with high large polaron mobilities for the Co-rich compositions at low temperatures, shifting towards small polaron mobilities with increasing Fe content. X-ray absorption spectroscopy (XAS) shows that Co is in a high spin state and takes on the main part of the cation oxidation state changes, and that hole states are in orbitals overlapping with the O 2p states, confirming the large polaronic behaviour, while holes on Fe are more localised at the cation. Hydration is more pronounced in inert atmospheres, as hydration of oxygen vacancies is easier than hydrogenation and increases with Fe content, in line with the commonly accepted finding that delocalization of holes disfavours protonation. Fe-rich compositions benefit from lower TCEC and higher hydration and hence expected proton permeability, at the cost of lower electronic conductivity. The surfaces are hydrophobic irrespective of Fe content, suggesting weak chemisorption of the underlaying water layer, possibly giving relatively many available surface sites for oxygen adsorption, but limited surface proton conductance – both of importance to positrodes for *operando* PCECs.

1. Introduction

Mixed protonic-electronic conductivity is essential in positrodes for Proton Ceramic Fuel Cells (PCFCs)[1] and Steam Electrolysers (PCSEs) [2]. Leading materials are perovskite cobaltites and ferrites exhibiting also oxide ion conduction (through oxygen vacancies)[1,3–5]. Cobaltites and ferrites exhibit catalytic activity for the oxygen evolution reaction[6], water splitting[7], ammonia synthesis[8], methane reforming[9], water purification by decomposition of organic pollutants [10], diesel soot combustion and other exhaust processing in the automotive industry[11]. The concentration and transport of protons (H^+) appear important in a many of them and also surface protonics can enhance the performance of many catalysts[12]. Works by Zohourian et al. [1]. and Raimondi et al. [13]. report considerable hydration of doped barium and strontium ferrites with proton concentrations peaking at 10 mol% for $Ba_{0.95}La_{0.05}Fe_{0.8}Zn_{0.2}O_{3-\delta}$.

In our recent works[4,14,15], we analysed the dissolution of protonic defects and the electronic properties of barium lanthanide (*Ln*) cobaltite perovskites. These materials can crystallize either in simple cubic perovskite structure with general formula $Ln_{0.5}Ba_{0.5}CoO_{3-\delta}$, or in the so-called double perovskite structure with formula $BaLnCo_2O_{6-\delta}$. In the former, Ln and Ba are randomly distributed on the A-site, with Ba^{2+}

---

* Corresponding author.
E-mail address: sebastian.wachowski@pg.edu.pl (S.L. Wachowski).

https://doi.org/10.1016/j.actamat.2024.120585
Received 26 September 2024; Received in revised form 5 November 2024; Accepted 20 November 2024

acting as an acceptor substituent for the host Ln^{3+}, hence we adopt the formula $Ln_{0.5}Ba_{0.5}CoO_{3\text{-}\delta}$ as more appropriate than the commonly used $Ba_{0.5}Ln_{0.5}CoO_{3\text{-}\delta}$. In the double perovskites, Ba and Ln are ordered in alternating layers along the c axis resulting in the doubling of the unit cell, and $BaLnCo_2O_{6\text{-}\delta}$. Our survey[4] and other literature[16] on water uptake in these compounds show that members where Ln is La or Gd or a mixture of those are prone to dissolve protons. On the other hand, there is a correlation that more basic cations on the B-site of mixed conducting perovskites increase the proton solubility[1,13]. Therefore, one may expect that substitution of Co with the more basic Fe will increase the proton concentration in barium lanthanide cobaltites. Furthermore, a recent study of ours indicates that protons dissolve in $La_{0.5}Ba_{0.5}Co_{0.5}Fe_{0.5}O_{3\text{-}\delta}$ and significantly affect its electronic conductivity [17]. This substantiates the importance of studying the properties of a mixed conductor in a system where the Co to Fe ratio on the B-site of the perovskite structure is changed. An additional advantage of exchanging Co with Fe is lowering the high thermal and chemical expansion of the cobaltites, which may limit their applicability due to thermal mismatch with other components of the devices[18]. On the other hand, both ferrites and cobaltites are good mixed oxide ionic and electronic conductors[19–25] with high catalytic activity, and hence the Fe substitution should maintain these properties while improving the solubility and minority conduction of protons.

This work presents an extensive study of the relation between the iron content and the structural and electrical properties of $La_{0.5}Ba_{0.5}Co_{1\text{-}x}Fe_xO_{3\text{-}\delta}$, with emphasis on the thermodynamics of hydration and oxidation, electronic structure, their relationship with the conductivity, and thermal and chemical expansion.

2. Experimental

$La_{0.5}Ba_{0.5}Co_{1\text{-}x}Fe_xO_{3\text{-}\delta}$ (x = 0.0, 0.25, 0.5, 0.75, 1.0) were synthesized with solid state reaction, starting with La_2O_3 (99.99 % Alfa Aesar, preheated at 900 °C for 5 h), $BaCO_3$ (99.9 % Sigma Aldrich), Co_3O_4 (99.9 % Sigma Aldrich) and Fe_2O_3 (99.9 % Sigma Aldrich). The stoichiometric amounts of powders were hand mixed and ground in an agate mortar with isopropyl alcohol as a medium, pelletized and annealed during the two-stage process at 1100 °C and 1200 °C for 48 h in an ambient air atmosphere with intermediate regrinding. In order to obtain $La_{0.5}Ba_{0.5}FeO_{3\text{-}\delta}$ an additional ball milling (20 h at 450 rpm) was applied before the first annealing and the temperature of the first step was increased to 1200 °C. The nomenclature used for the sample description is presented in Table 1.

The structural characterization was performed by X-ray diffraction (XRD) using an X'Pert Phillips diffractometer with Cu Kα radiation (1.541 Å). The diffraction patterns were analysed by Rietveld refinement using GSAS-II[26] software.

The initial oxygen content of the synthesized oxides was determined by iodometric titration. 15–20 mg of each sample and a surplus of potassium iodide (ca. 0.2 g) were put in a three-neck flask and flushed with nitrogen. When the air was removed, 15 ml of 2 M HCl was added to dissolve the specimen. The iodine ions were titrated with starch as an indicator under an inert atmosphere with 0.01 M sodium thiosulphate aqueous solution using a 10 ml microburette (±0.05 ml). The oxygen content calculated from this study was used as an initial point of analysis of the oxidation process by thermogravimetry (TG).

Table 1
The nomenclature used for sample description.

Composition	Label
$La_{0.5}Ba_{0.5}CoO_{3\text{-}\delta}$	LBC
$La_{0.5}Ba_{0.5}Co_{0.75}Fe_{0.25}O_{3\text{-}\delta}$	LBCF25
$La_{0.5}Ba_{0.5}Co_{0.5}Fe_{0.5}O_{3\text{-}\delta}$	LBCF50
$La_{0.5}Ba_{0.5}Co_{0.25}Fe_{0.75}O_{3\text{-}\delta}$	LBCF75
$La_{0.5}Ba_{0.5}FeO_{3\text{-}\delta}$	LBF

Thermogravimetry (TG) was performed to study oxygen content using a Netzsch Tarsus 401 thermobalance. We analysed the temperature evolution of oxygen nonstoichiometry isobarically in a synthetic air atmosphere in the temperature range RT-900 °C, with a temperature ramp rate of 2 °/min during both cooling and heating.

The thermochemical expansion coefficient was analysed using a Netzsch DIL 402 PC/4 dilatometer. For dilatometry and electrical conductivity studies the powders were pressed into a rectangular sample (25×5 × 4) mm under 1.8 GPa pressure and sintered at 1150 °C for 24 h with 2 °C/min heating and cooling rates. Relative density of as prepared pellets exceeded 90 % for all of the investigated materials. For dilatometry, the bars were shortened to about 15 mm. The relative length change was measured as a function of temperature during the cooling of the samples from 1000 °C to room temperature in dry synthetic air.

Electrical conductivity measurements were conducted by standard four-point DC technique on the sintered rectangular bars using silver wire and paste for contacting. The measurements were carried out in a temperature range from 800 to 100 ºC by cooling down (1 ºC/min) in constant atmospheres. Several O_2-containing atmospheres were tested (pO_2 = 1, 0.21, 0.05, 0.1, 0.01, 0.001) in addition to nominally O_2-free Ar. A constant current was supplied by a programmable current source (Keithley 2601) and the voltage drop was measured by a multimeter (Keithley 3706). Once the highest temperature (800 ºC) was reached, the samples were left to stabilize for 2 h in order to ensure the high-temperature redox state corresponding to the specific pO_2.

X-ray absorption spectroscopy measurements were performed in fluorescent mode at the Solaris National Synchrotron Radiation Centre in Kraków, Poland. A dedicated PEEM/XAS bending magnet beamline was utilized to measure Re-$M_{4,5}$, Co-$L_{2,3}$, Fe-$L_{2,3}$, and O-K edges. Powders of samples were mounted on carbon tape and placed on the Omicron plates for measurements.

Hydration studies were performed using a Netzsch Jupiter® 449 F1 thermal analyser. The as-prepared powders were heated to 800 °C (5 °/min) and held at this temperature for 5 h under dry air. After drying, the samples were cooled to 300 °C in dry gas (5 °/min). After 2 h of stabilization, the dry purge gas was switched to the humidified gas (pH_2O = 0.023 atm), then after additional 2 h, the purge gas was switched back to the dry gas. The experiment was performed under two different pO_2 conditions: either synthetic air or nitrogen. At lower pO_2 slow equilibration with oxygen at 300 °C affected the baseline of the hydration studies. Therefore, an additional mathematical correction of the baseline was done. The details of the data processing and the data before and after correction are given in SI.

An Autosorb IQ apparatus was used to measure both H_2O and N_2 adsorption isotherms. Samples were degassed at 300 °C for 3 h in vacuum prior to each measurement. N_2 adsorption isotherms were used to determine specific surface area. They were measured at 77 K with the relative pressure (p/p_0) changed from 0.05 to 0.9. Based on the obtained data, specific surface area was calculated using the BET linear equation. The correlation coefficient of the linear regression was not <0.99. The water adsorption measurements were performed at RT in the relative pressure range (p/p_0) from 0.05 to 0.9.

3. Results and discussion

3.1. Structural analysis

As indicated by the XRD patterns shown in Fig. 1a all $La_{0.5}Ba_{0.5}Co_{1\text{-}x}Fe_xO_{3\text{-}\delta}$, ($x$ = 0.0, 0.25, 0.5, 0.75, 1.0) were single phase cubic perovskites (space group $Pm\overline{3}m$). An exemplary Rietveld refinement profile of $La_{0.5}Ba_{0.5}Co_{0.25}Fe_{0.75}O_{3\text{-}\delta}$, is shown in Fig. 1b. (For more refinements see the supplementary information S1-S4.) The results of the refinements are given in the SI Table 1. Unit cell parameters were obtained from the refinement, and as shown in Fig. 1c, the unit cell parameter a increases nonlinearly with the iron concentration. To create an "upward"

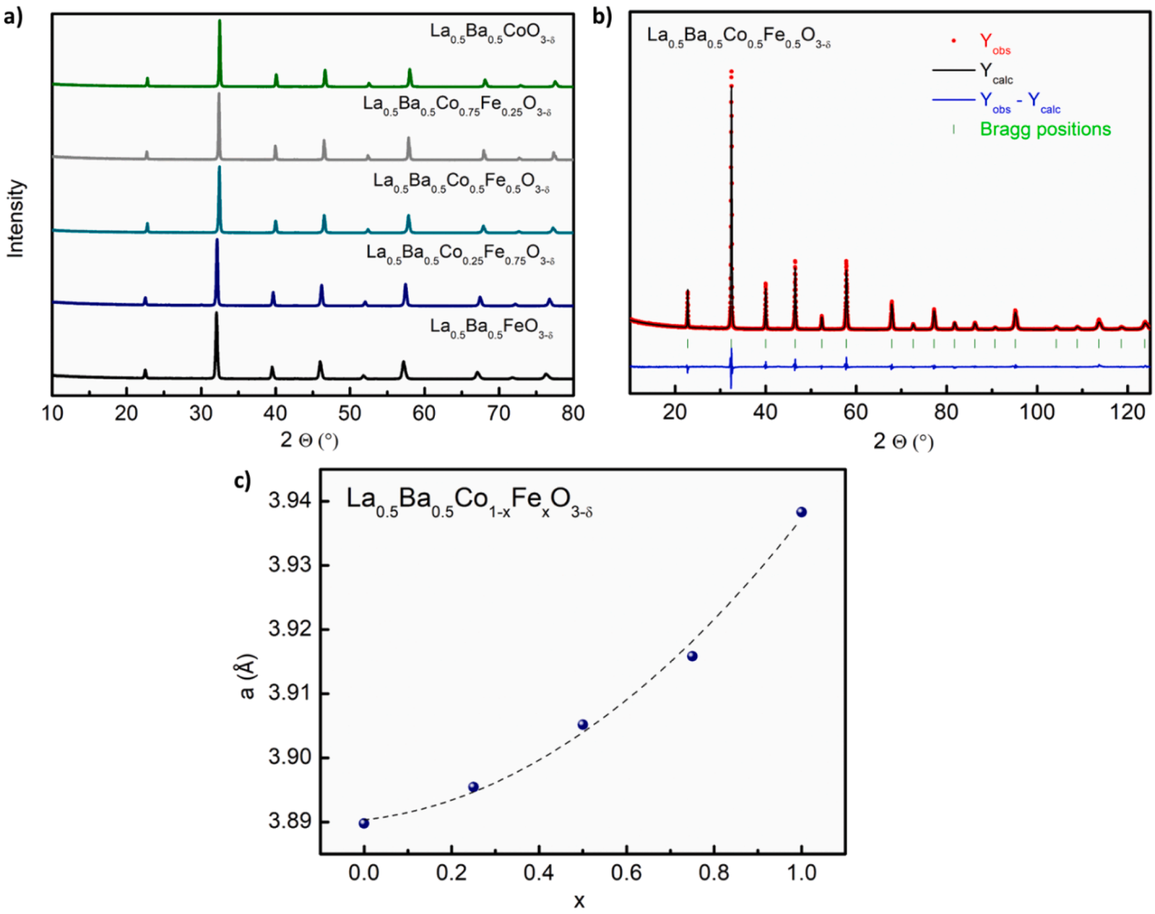

Fig. 1. Characterisation of compounds cooled down at 3 °C/min from synthesis in ambient air: XRD patterns for compounds with different iron content (a), representative diffraction pattern with Rietveld refinement profile (b), the dependence of lattice parameter on iron content (c).

deviation from linearity the substitution must be accompanied with an additional increase of B-site cation radius. This could be caused by the reduction of the average oxidation state and/or increase the spin state of the B-site cations as both of these effects cause an increase in the ionic radius. A similar nonlinearity has been observed in different perovskite ferrites[27].

3.2. *Oxygen content and oxidation state: Iodometric titration and TG*

The thermal evolution of the oxidation state measured by TG in synthetic air is presented in Fig. 2a, with the averaged oxidation state from iodometric titration taken as initial value at room temperature. The oxygen content remains unaffected with increasing temperature up to roughly 300 °C, expectedly reflecting a combination of saturation and frozen-in oxygen content and lack of equilibrium. At higher temperatures the oxygen is released from the oxide and we may assume equilibrium with the atmosphere. Based on literature data, the diffusion constant for oxygen in perovskite cobaltites and ferrites is 10^{-8} cm^2/s or higher at temperatures 600-700 °C [28,29], justifying equilibrium with the grain sizes and times of the temperature steps in this study. The resulting van 't Hoff plots for all compounds are shown in Fig. 2b and above 600 °C display linear behaviours indicating equilibrium. Large variation of the slope and intercepts suggest that both enthalpies and pre-exponentials vary considerably with iron content.

The materials investigated here are cubic perovskites and hence $LaCoO_3$ and $LaFeO_3$ and their solid solutions must be taken as the reference compositions, with Co^{3+} ($3d^6$) and Fe^{3+} ($3d^5$) ions as the ground level unexcited states. The main defects will be the acceptor substituent $Ba_{La}^{/}$, oxygen vacancies $v_O^{\bullet\bullet}$, and electronic defects, namely electron holes representing Co^{4+} and Fe^{4+} states ($M_M^{\bullet}$) and electrons representing Co^{2+} and Fe^{2+} states ($M_M^{/}$). We will in the following hence apply the defect chemical approach provided by Malyshkin et al. [30]. for $La_{0.5}Ba_{0.5}CoO_{3\text{-}\delta}$, and the electroneutrality condition is then

$$2\left[v_O^{\cdot\cdot}\right] + \left[M_M^{\cdot}\right] = \left[Ba_{La}^{/}\right] + \left[M_M^{/}\right], \tag{1}$$

The equilibrium between the three variable defects can be described in terms of two reactions. The oxidation reaction can be written

$$\frac{1}{2}O_{2(g)} + v_o^{\cdot\cdot} + 2M_M^{x} = O_o^{x} + 2M_M^{\cdot}, \tag{2}$$

where O_o^x is a lattice oxide ion and $O_{2(g)}$ an oxygen gas molecule. The equilibrium coefficient is

$$K_{ox} = \frac{\left[O_o^x\right]\left(\frac{\left[M_M^{\cdot}\right]}{\left[M_M^{x}\right]}\right)^2}{\left[v_o^{\cdot\cdot}\right]\left(\frac{p_{O_2}}{p^0}\right)^{1/2}} = exp\left(\frac{\Delta S_{ox}^0}{R}\right)exp\left(\frac{-\Delta H_{ox}^0}{RT}\right). \tag{3}$$

The disproportionation of the transition metal cation may be written

$$2M_M^{x} = M_M^{\cdot} + M_M^{/}, \tag{4}$$

with equilibrium coefficient

$$K_{dis} = \frac{\left[M_M^{\cdot}\right]\left[M_M^{/}\right]}{\left[M_M^{x}\right]^2} = exp\left(\frac{\Delta S_{dis}^0}{R}\right)exp\left(\frac{-\Delta H_{dis}^0}{RT}\right). \tag{5}$$

Our equilibrium oxidation states and oxygen contents show that the

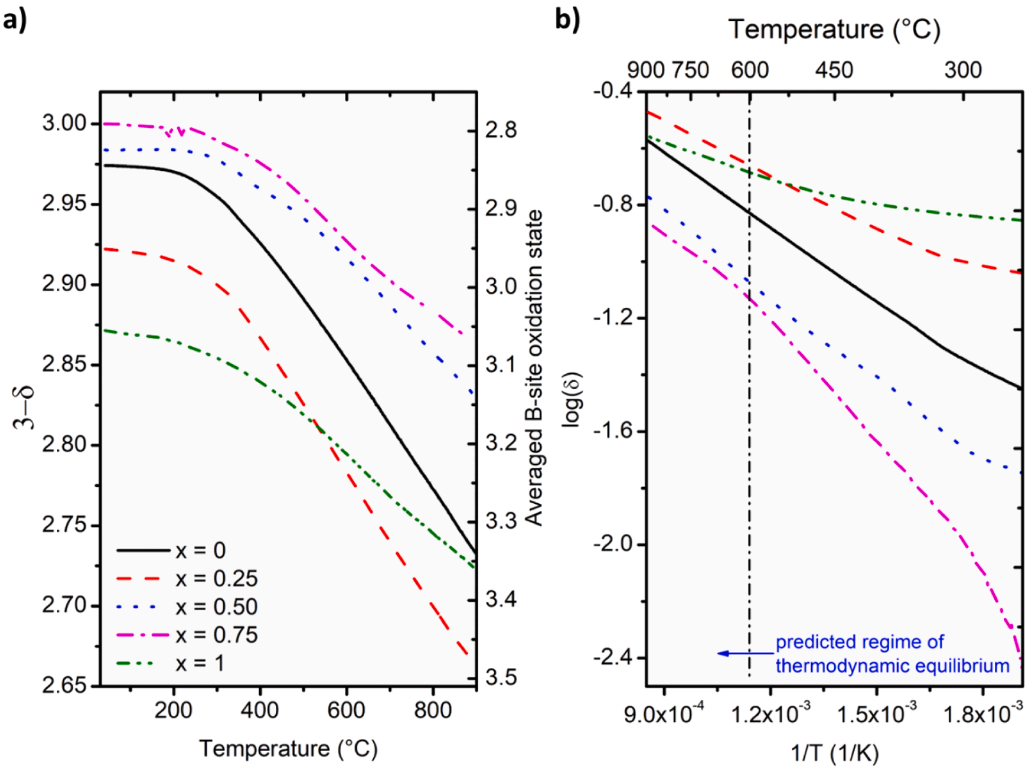

Fig. 2. Oxygen nonstoichiometry (3-δ) and averaged B-site oxidation state in synthetic air as a function of temperature upon cooling (a) and van 't Hoff plots of the concentration of oxygen vacancies (b).

oxidation reaction is in balance and that both electron holes and oxygen vacancies hence are significant positive defects. Moreover, the lack of levelling out at the oxidation state of 3 shows that the disproportionation is favourable and that electrons are also significant. Hence, the defect model and electroneutrality condition cannot be resolved into any simple limiting case, and we may not assign apparently straight lines in van 't Hoff plots to single thermodynamic parameters but have to solve the full set of equations. Malyshkin et al. [30]. derived an analytical expression of pO_2 as a function of temperature and oxygen content. Based on fits of the stoichiometry in $La_{0.5}Ba_{0.5}CoO_{3-\delta}$ as a function of pO_2 at 1000, 1050, and 1100 °C they found that $\Delta S^0_{ox} = -35.4 \pm 1.8$ J/molK and $\Delta H^0_{ox} = -50.9 \pm 2.1$ kJ/mol and assuming $\Delta S^0_{dis} \approx 0$ that $\Delta H^0_{dis} = 30.1 \pm 0.5$ kJ/mol. They further provided several literature references to earlier studies of the same material showing oxygen stoichiometries 3-δ in the air at room temperature in the range 2.9–3.0 and at 900 °C between 2.75 and 2.80. The numerical solution of the parameters by Malyshkin *et al* [30]. referred to above for $La_{0.5}Ba_{0.5}CoO_{3-\delta}$ qualitatively yields the non-stoichiometries we observe. Our non-stoichiometry data are not sufficiently extensive to fit thermodynamic parameters for our compounds.

3.3. *Thermochemical expansion*

Thermochemical expansion was studied in the air by dilatometry. Considering that all studied materials are thermally reduced above 300 °C one must consider the elongation as a combination of thermal and chemical expansion. Fig. 3a is a combined graph where the relative elongation as a function of temperature is overlaid on the oxygen content change under the same conditions. LBCF50 was chosen as a representative of the series – the other plots can be found in SI part 6. At low temperatures the thermal expansion is linear, which corresponds to a constant oxygen content below 300 °C. Above this temperature the expansion increases as the oxygen is released and therefore the elongation is of a thermochemical nature[4]. Thus, all compounds have a total ThermoChemical Expansion Coefficient (TCEC) significantly higher at high than at low temperatures. The values of the TCECs at low and elevated temperatures are plotted as a function of *x* in Fig. 3b. What is the most important from the application point of view is that in both low and high temperature ranges the expansion coefficient decreases with increasing iron content, especially for the low temperature part where α is reaching the value $11 \bullet 10^{-6}\ K^{-1}$. Such thermal expansion coefficients should be compatible with BZCY electrolyte materials for which it is reported in the range of $7\text{–}11 \bullet 10^{-6}\ K^{-1}$ [18].

Further analysis can be done to evaluate how chemical expansion contributes to the total expansion. Knowing the approximate temperature at which the reduction starts, the thermal and chemical expansion can be separated. At low temperatures the oxygen stoichiometry of the material remains constant (frozen in) and the expansion is purely thermal. Assuming that the thermal expansion coefficient (α) is approximately constant in the whole studied temperature range, the chemical expansion related to a change in oxygen stoichiometry may be evaluated as a difference between the total expansion and the thermal one. A similar approach has been applied in other studies[14,18]. The relative elongation, with the subtracted thermal expansion component, plotted as a function of oxygen nonstoichiometry δ, is shown in Fig. 3c. The chemical expansion coefficient of reduction β_{red} resulting from thermal reduction is determined by the relation[18]:

$$\beta_{red} = \frac{1}{\delta} \cdot \frac{dl_{chem} - l_0}{l_0} \tag{6}$$

where dl_{chem} is the change in length due to chemical expansion only (thermal component is subtracted), l_0 is the initial length of the sample. The values of α and β are given in Table 2.

3.4. *Electrical conductivity*

Fig. 4 presents the electrical conductivity as a function of pO_2 for all sample compositions at 400, 600, and 800 °C. Such isotherms give direct

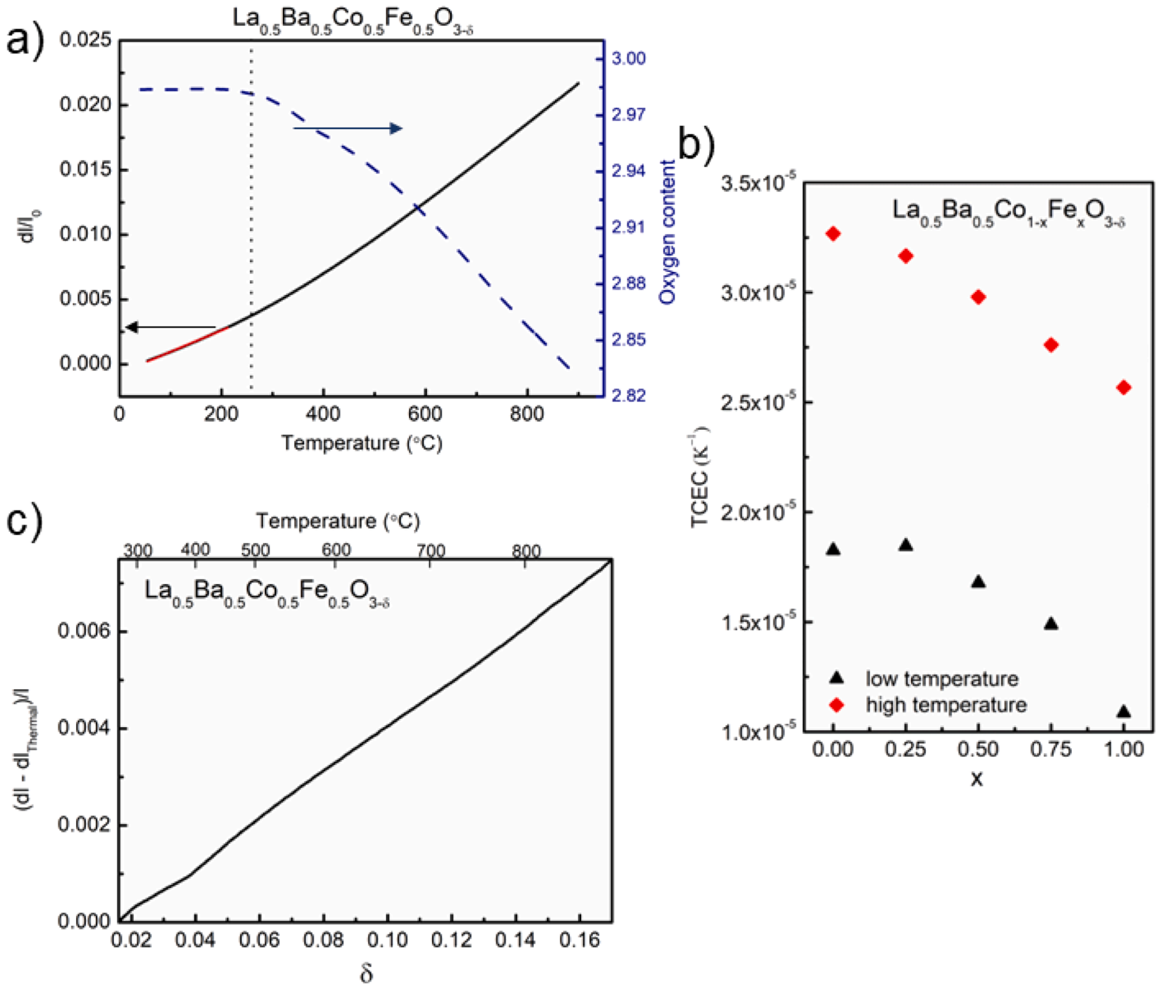

Fig. 3. Temperature dependence of oxygen content (3-δ) and relative length change of LBCF50 (a), total thermochemical expansion coefficient (TCEC) at low and high temperature (b), relative length change of LBCF50, with subtracted thermal expansion, as a function of oxygen nonstoichiometry (c).

Table 2
Thermochemical, thermal, and chemical expansion coefficients of reduction of LBCFs.

Compound	$TCEC_{>300\,^\circ C}$ $(10^{-6}\ K^{-1})$*	α $(10^{-6}\ K^{-1})$*	β_{red}
LBC	32.7(3)	18.3(3)	0.037(8)
LBCF25	31.7(2)	18.5(2)	0.033(7)
LBCF50	29.8(2)	16.8(2)	0.048(4)
LBCF75	27.6(2)	14.9(2)	0.054(5)
LBF	25.7(2)	10.9(3)	0.059(5)

* $TCEC_{<300\,^\circ C} = \alpha$ since in this temperature regime TCEC consists only of the thermal part.

information about the variations in the concentration of charge carriers. The high conductivity in these acceptor-substituted materials as well as the consistent increase in conductivity with pO_2 shows that the charge carriers can be considered to be electron holes, in line with a positive Seebeck coefficient found for $BaGd_{0.8}La_{0.2}Co_2O_{6\text{-}\delta}$ [5], a compound closely related to LBC.

We see directly that the conductivity decreases with increasing Fe content x, reflecting as we shall see mainly the decreasing mobility of electron holes. The isotherms at the lowest temperature (400 °C) level out at high pO_2, showing that the material approaches full oxidation, where the concentration of holes equals that of Ba acceptors, i.e., 0.5 per formula unit, and the oxygen deficiency δ is close to zero. At lower pO_2, the conductivity drops, reflecting a decrease in the hole concentration and increasing oxygen deficiency δ. As we go to higher temperatures (600 and 800 °C), we see a decreasing tendency of oxidation, as expected from the thermodynamics of Reaction (2). This tendency appears stronger with increasing Fe content. Under the limiting case solution to Eq. (3) meaning that oxygen vacancies have become dominating and compensating the acceptors while holes are the minority, the slope should approach ¼, reflecting a $pO_2^{1/4}$ dependence. This is by and large obeyed, but the Fe-rich samples show a tendency at low pO_2 and temperature to take on higher slopes. We suspect that this may reflect the ordering of the structure due to high oxygen vacancy concentrations.

Fig. 5 shows temperature dependencies of the conductivities of selected samples under oxidising or reducing conditions (data for all samples are available in the SI, *cf*. Figures S13–19). In interpreting these, the conductivity of holes is the product of charge, concentration, and charge mobility according to

$$\sigma = Fuc = Fu[\mathrm{h}^{\cdot}]c_{\mathrm{m}} = Fu\left[M_M^{\cdot}\right]c_{\mathrm{m}} \tag{7}$$

where $[\mathrm{h}^{\cdot}]$ and $\left[M_M^{\cdot}\right]$ represent the molar ratio concentration of holes and polarons and c_{m} is the molar concentration (molar density) of the $LaMO_3$ perovskite. In a very first approximation, the charge mobility u reflects the harmonic (inverse) sum of the inverse charge mobilities representing different ways to trap (**s**mall **p**olaron, **l**arge **p**olaron) or scatter (**ph**onon, **imp**urity) the hole:

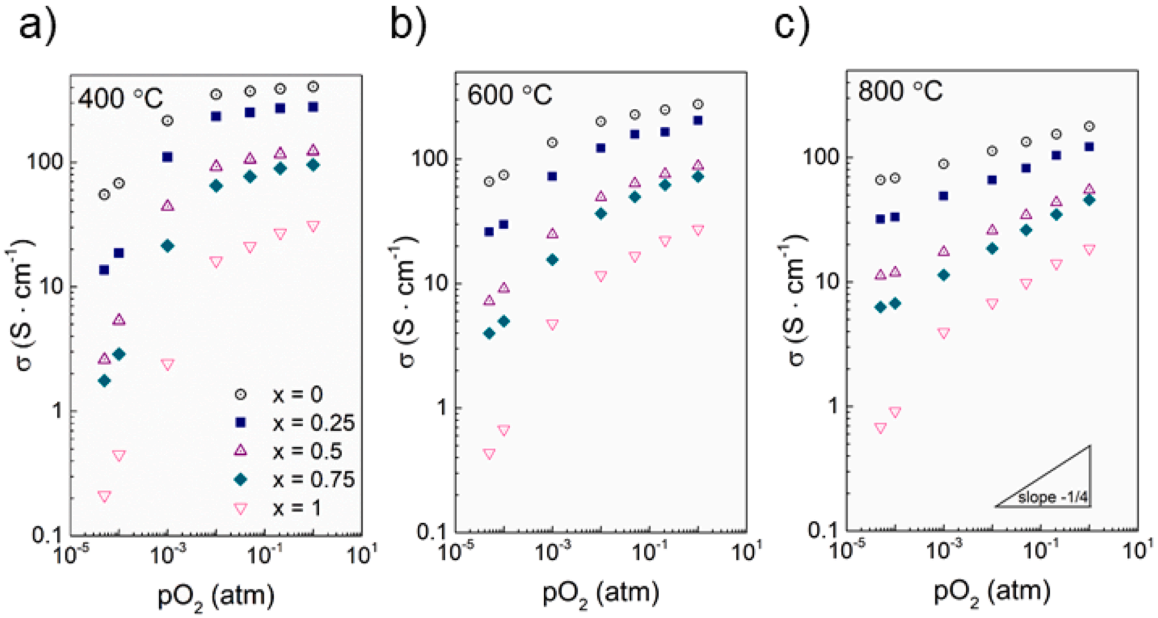

Fig. 4. Conductivity of $La_{0.5}Ba_{0.5}Co_{1\text{-}x}Fe_xO_{3\text{-}\delta}$ plotted as a function of oxygen partial pressure at three selected temperatures: 400 °C (a), 600 °C (b) and 800 °C (c).

$$u = \frac{1}{\frac{1}{(1-[M_M^{\cdot}])u_{\mathrm{sp}}} + \frac{1}{u_{\mathrm{lp}}} + \frac{1}{u_{\mathrm{ph}}} + \frac{1}{u_{\mathrm{im}}}} = \frac{1}{\frac{1}{(1-[M_M^{\cdot}])u_{\mathrm{sp}}^0 \frac{1}{T} e^{\frac{-\Delta H_{\mathrm{m}}}{kT}}} + \frac{1}{u_{\mathrm{lp}}^0 T^{-1/2}} + \frac{1}{u_{\mathrm{ph}}^0 T^{-3/2}} + \frac{1}{u_{\mathrm{im}}^0 T^{+3/2}}}. \tag{8}$$

Here, we have included the term $(1-[M_M^{\cdot}])$ for small polarons as the probability to find a neighbouring M^{3+} or M^{2+} to jump to, but omitted similar terms for the other mechanisms. The conductivities under oxidising conditions – especially of the Co-rich samples – are relatively independent of temperature. Here, the concentration of charge carrying electron holes is close to constant and the plots yield information about charge mobility. Arrhenius plots of $\ln\sigma$ or $\ln(\sigma T)$ vs 1/T to extract activation energies would in these cases give negative, negligible, or (in the case of $\ln(\sigma T)$ vs 1/T plots) slightly positive values only reflecting the T in the $\ln(\sigma T)$ expression. This means that migration is not an activated small polaron process with deep self-traps, but a large polaron process with shallow self-traps or an itinerant process with impurity or lattice phonon scattering. Fig. 5a) compares $\log(\sigma)$ vs $\log(T)$ and $\log(\sigma)$ vs 1/T for all samples in oxidising conditions (air, $pO_2 = 0.21$ atm). For LBC, the plot shows a $\sigma = \sigma_0 T^{-1/2}$ dependency at low temperatures, reflecting under these conditions the charge mobility of holes, in agreement with the expectancy of large polaron transport [31]. Inserting this into Eq. (7) with $c_{\mathrm{m}} = 0.028$ mol/cm^3 and $[M_M^{\cdot}] = [\mathrm{Ba}_{\mathrm{La}}^{/}] = 0.5$, we obtain $u_{\mathrm{lp}} = u_{\mathrm{lp}}^0 T^{-1/2}$ with $u_{\mathrm{lp}}^0 = 18{,}000$ cm^{2}K$^{1/2}$/sV for the large polaron charge mobility of holes in LBC.

At higher temperatures, the conductivity takes on a steeper decrease, as expected for lattice phonon scattering, nominally with a $u_{\mathrm{ph}} = u_{\mathrm{ph}}^0 T^{-3/2}$ dependence of charge mobility in LBC in air. As temperature increases further, the slope gets more negative, suggesting that the concentration of carriers decreases significantly due to the onset of reduction, in line with the pO_2 dependence for this sample at the highest temperatures. At the lowest partial pressures of oxygen, where the conductivity takes on a $pO_2^{1/4}$ dependence, and at the lowest temperatures of 400 °C and below, the conductivity takes on an Arrhenius behaviour with enthalpies of 47 kJ/mol for LBC (*cf.* Fig. 5c and 5d). This should reflect the enthalpy of small polaron migration and half the enthalpy of oxidation, which is −50.9 kJ/mol, yielding an enthalpy of small polaron migration of as much as 73.5 kJ/mol for LBC. Alternatively, the sample may not be able to take up equilibrium amount of oxygen during cooling in the atmospheres with the lowest oxygen contents (10^{-4} and 5×10^{-5} atm), so that the activation enthalpy of conductivity reflects solely the small polaron hopping enthalpy.

With increasing Fe content we see in more cases an increase of conductivity with the temperature dep at low temperatures under oxidising conditions, attributable to more localised holes and that the activation enthalpy of the small polaron mobility overtakes the loss of electron holes with increasing temperature. At the lowest oxygen activities, distinct activation energies around 30 kJ/mol are observed, reflecting a minimum of the small polaron hopping enthalpy. At the highest temperatures, the conductivities of the Fe-rich samples decrease, as the loss of holes due to reduction overcomes the increasing small polaron mobility.

3.5. Electronic structure

X-ray absorption spectroscopy of the O K edge and $L_{2,3}$ edges was studied to reveal the electronic structure of the transition metals as well as the nature of chemical bonding between the transition metal and oxygen. Since all compounds are nearly fully oxidized we limit the analysis to octahedral coordination where six oxide ions surround the B-site cation in the perovskite structure. In such a case the orbital energies split into two e_g orbitals with higher and three $t_{2\,g}$ orbitals with lower energy. The metal cations can have two or three different electron configurations at these $t_{2\,g}$ and e_g orbitals for each oxidation state. For instance, a metal cation with a $3d^6$ configuration such as Co^{3+} or Fe^{2+} can have High Spin (HS) $t_{2g}^4 e_g^2$, Intermediate Spin (IS) $t_{2g}^5 e_g^1$, or Low Spin (LS) $t_{2g}^6 e_g^0$ states. Empty states at $t_{2\,g}$ levels, typical for higher spin configurations, are usually considered as electron holes in the literature [32, 33].

Fig. 6a shows the X-ray absorption spectra of the O K edge. The first peak, labelled as A, results from the transition from O 1 s core energy level to the hybridized orbital consisting of a 3d level of transition metal and the O 2p level. This transition is of particular interest in cobaltites since it gives information on the occupancies of 3d $t_{2\,g}$ and e_g and O 2p ligand states. The magnification of the 526–532 eV energy range with the first derivative of normalized absorption is presented in Fig. 6b. The intensity of the first peak, reflecting t_{2g}-O 2p overlap, is the highest, which represents the highest concentration of the unoccupied $t_{2\,g}$ states,

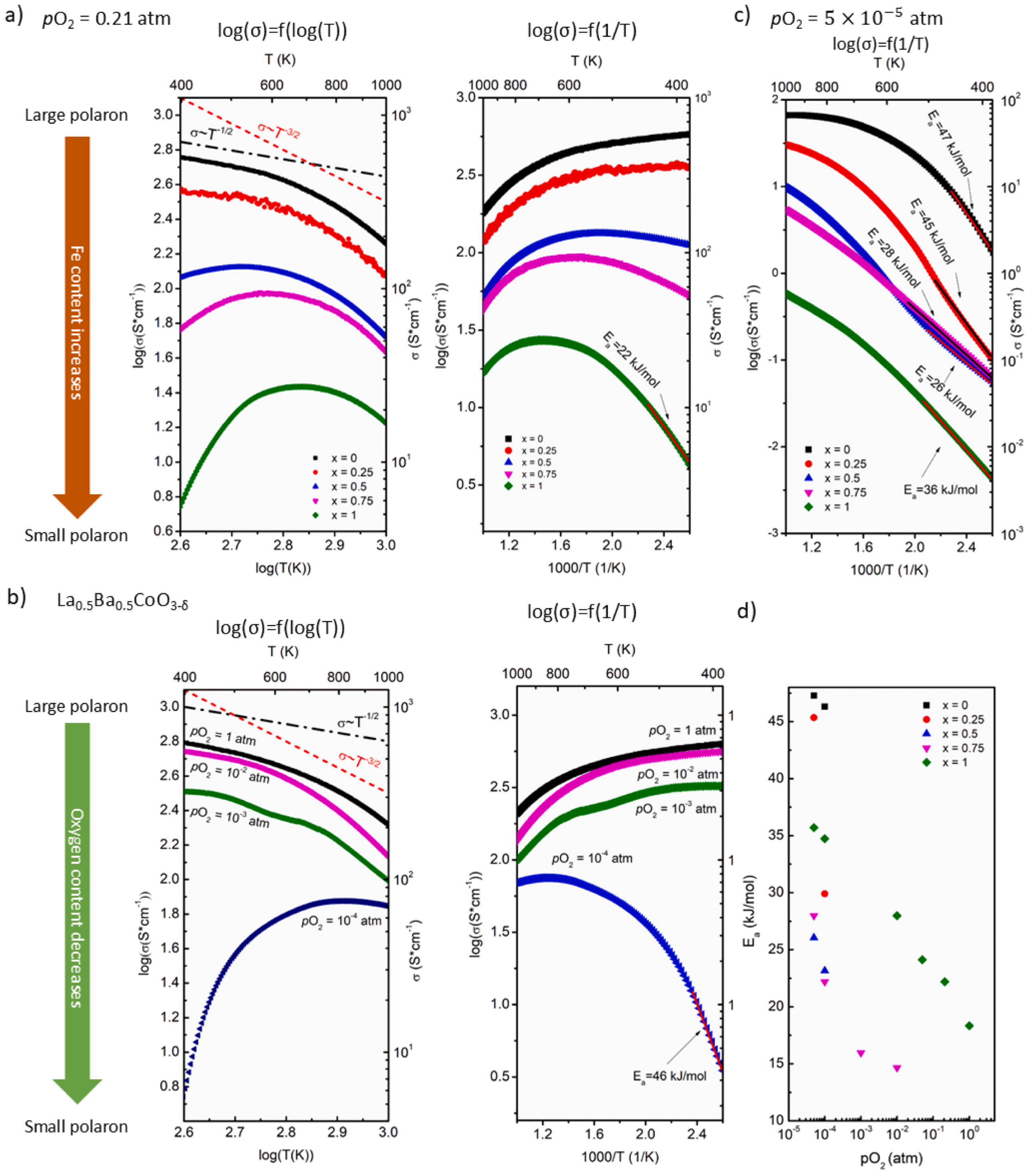

Fig. 5. Conductivity data plotted for selected samples using various models: a) log(σ) as a function of log(T) and as a function of $1/T$ for the different samples in air, b) log(σ) as a function of log(T) and as a function of $1/T$ for $La_{0.5}Ba_{0.5}CoO_{3\text{-}\delta}$ in various pO_2 conditions (the dashed lines in a) and b) are simulated curves of $\sigma \propto T^{-\frac{1}{2}}$ or $\sigma \propto T^{-\frac{3}{2}}$ dependencies as guide for the eyes, only), c) log(σ) as a function of $1/T$ plotted for data gathered at $pO_2 = 5 \times 10^{-5}$ atm (the solid lines indicate the ranges in which the activation energies are calculated from ln(σT) vs $1/T$), and d) activation energies obtained at low T representing enthalpy of mobility of small polarons plotted as a function of pO_2.

which in turn represents, on average, the highest spin state. The shift towards higher energies in the position of the pre-peak (Fig. 6c) observed with increasing iron content reflects the decrease of covalency in the bond between the transition metal and the oxygen [34]. O K pre-edge spectra reflect the unoccupied p-projected density of states (DOS) of the cations, thus the spectral weight gives information on the density of unoccupied states. The spectral weight of this peak decreases significantly with increasing iron content, which means that the concentration of holes delocalized from the B-site cation to the oxide ions decreases. This corresponds well with the analysis of the electrical properties: as Fe content increases the conductivity decreases due to more localized holes and lowered hole concentration. The higher energy

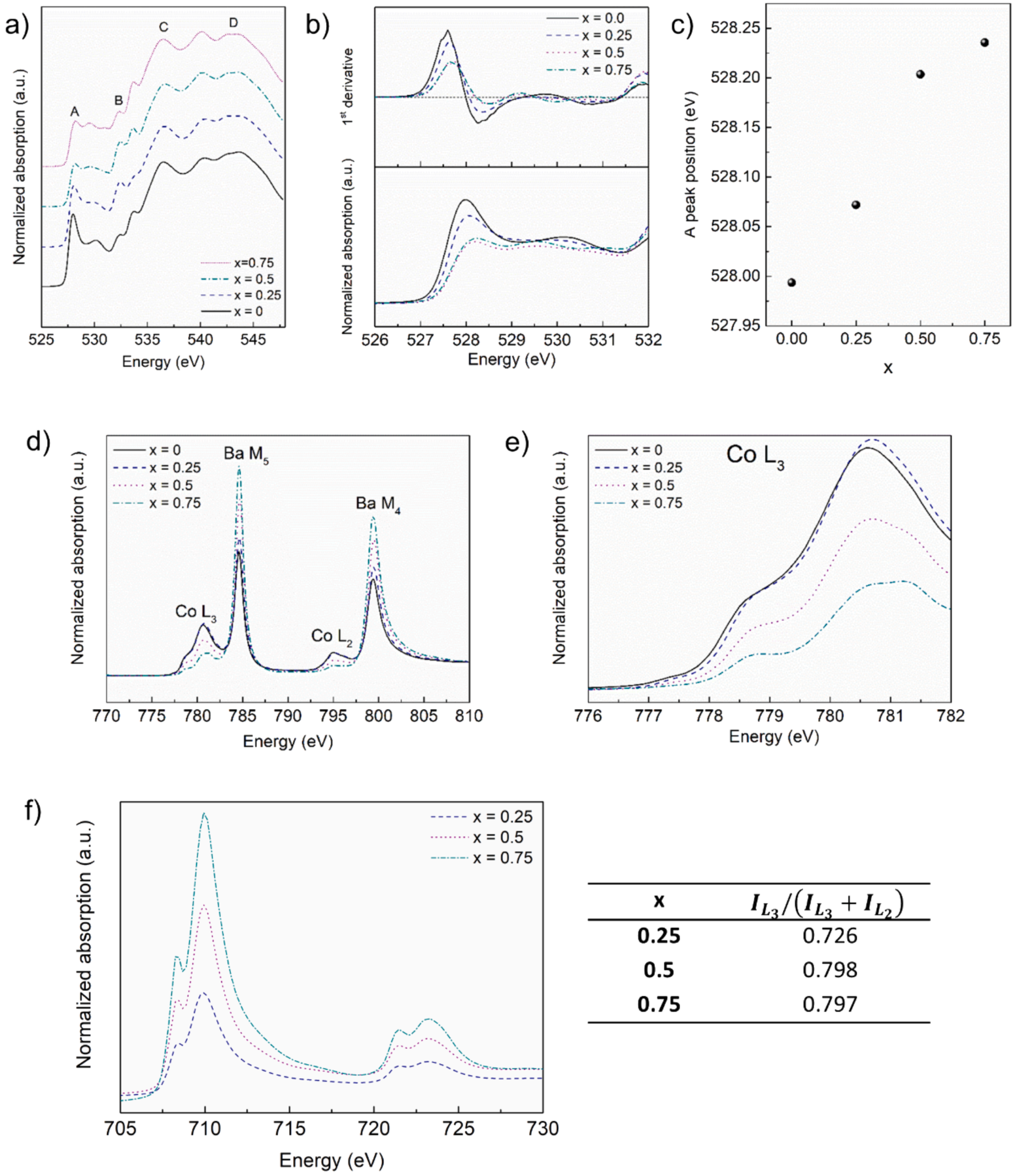

x	$I_{L_3}/(I_{L_3}+I_{L_2})$
0.25	0.726
0.5	0.798
0.75	0.797

Fig. 6. X-ray absorption spectroscopy of $La_{0.5}Ba_{0.5}Co_{1\text{-}x}Fe_xO_{3\text{-}\delta}$. O K XANES of BLCFs (a), X-ray absorption spectra of oxygen K-edge pre-peak structure and 1st derivative of normalized absorption of oxygen K-edge pre-peak structure (b), the A peak position as a function of iron content (c), X-ray Absorption Spectroscopy spectra of Co $L_{2,3}$ and Ba $M_{4,5}$ edges (d), X-ray Absorption Near Edge Structure spectra of Co L_3 edge (e), X-ray absorption spectra of Fe $L_{2,3}$ edges with calculated branching ratio (f).

ranges, in Fig. 6 denoted as C and D, give information on Ba 5d and transition metal 4sp unoccupied states[35], however, they do not provide key information on materials properties. The presence of a B peak may indicate surface contamination[35].

The oxidation state and spin state of cobalt and iron may also be investigated on transition metal $L_{2,3}$ edges as presented in Fig. 6e and 6f for Co and Fe, respectively. The $L_{2,3}$ spectra of transition metals arise from transitions from an initial configuration $2p^m d^n$ to the final configuration $2p^{m-1}d^{n+1}$, which is controlled by the selection rules $\Delta L = \pm 1$, $\Delta S = 0$. The spin-orbit interaction of the core hole with the valence electrons results in two multiplet structures[35] . The maximum of Co L_3 spectra (Fig. 6e) is observed above 780 eV while that of Co^{3+} is known to be below 780 eV [35,36], which indicates that a significant part of Co is at the +4 oxidation state. With increasing Fe content the maximum shift towards higher energies indicating increase of the Co^{4+} contribution. The low energy shoulder of Co L_3 indicates the high spin of cobalt.

The Fe $L_{2,3}$ spectra (Fig. 6f) do not change much with the iron content, suggesting that the Fe^{3+}/Fe^{4+} ratio remains essentially unaltered. The broadening of the reflections in relation to the Fe^{3+} spectrum indicates the presence of a mixture of Fe^{3+} and Fe^{4+}. Despite the negligible differences in the peak location, its spectral weight indicates the differences in a spin state which can be quantified with the branching ratio. This parameter, calculated from peak integrated intensities according to the ratio $\frac{I_{L_3}}{(I_{L_3}+I_{L_2})}$, describes the fractional probability for transitions from L_3 level, and is presented for the Fe $L_{2,3}$ peaks in Fig. 6. The branching ratio is close to unity which indicates high spin configurations[35]. Moreover, the ratio is similar for all compounds and virtually unchanged for BLCF50 and BLCF75. This suggests that Fe spin states do not change with varying Fe content either and most of the changes are due to changes in the Co states.

To sum up, with increasing Fe content the holes become more localized on the B-site explaining the change from large polaron transport in LBC to small polaron hopping in LBCFs and LBF. The Fe oxidation state is mixed 3+ and 4+ and primarily high spin for all samples. The Co oxidation state slightly increases to 4+ upon Fe substitution, which may partially explain the deviation from Vegard's law in Fig. 1. It is not clear how the spin state of Co is affected by the substitution, but it is mostly the HS configuration.

3.6. *Bulk protonation*

To analyse the hydration thermodynamics the mass change was recorded with a thermobalance at a constant temperature of 300 °C upon switching from dry ($p_{H2O} < 10^{-5}$ atm) to wet ($p_{H2O} \approx 0.01$ atm) conditions. The experiment was conducted both in oxidizing (synthetic air, $pO_2 = 0.2$ atm) and inert conditions (nitrogen, $pO_2 = 10^{-6}$ atm). Mass increase after exposure to humidified atmosphere indicates hydration (uptake of H_2O as $2H^+$ and O^{2-}), hydrogenation (uptake of H^+ and e^-) or hydroxidation (uptake of OH^- and h^+). An increase in mass was observed in all the investigated compositions under both air and inert atmosphere, see Fig. 7a and 7b, respectively, varying with atmospheres and sample iron content. Regardless of the actual reaction driving the water uptake, protonic concentrations were estimated assuming a hydration reaction for all conditions and the values are shown in Fig. 7c. The values are not representing the actual proton concentration, but merely serve as an indicator of the order of magnitude of protonic defect concentration that can be expected in such compounds.

In air, the mass increase during hydration of LBC is slow, as observed before for various barium lanthanide cobaltites[4]. It does not reach equilibrium after 2 h at 300 °C and appears not to be reversible. By increasing the substitution of Co by Fe, the total mass gain first decreases, reaching a minimum for LBCF25 and then increasing all the way to LBF. Furthermore, a faster and partly reversible process adds increasingly from 75 % Fe on, so that Fe-rich samples display a dual mass increase: one slow and irreversible superimposed on a fast and partly reversible, the latter typical of hydration or hydrogenation reactions for many oxides[1,4,25,27]. Under nitrogen atmosphere (Fig. 7b), the samples exhibit similar dual-time constant and fully or partly irreversible features as in air, but mass gains are in all cases higher. The tendency of Fe-rich materials to be more hydrating under both oxidising and inert atmosphere is clear.

On this basis, we divide the mass increase into two processes: The slow one is fairly independent of Fe content and is believed to reflect oxidation (or hydroxidation) accompanied by slow partial rearrangement of cations and the local structure. The fast process is regular hydration or hydrogenation, which is counteracted by holes delocalised to oxide ions (ligand holes): Co-rich compositions have more delocalised holes (large polarons) and oxide ions are not available for protonation (except after rearrangement of local structure). Fe-rich compositions have localised holes (small polarons) that leave oxide ions more available for protonation. Inert atmospheres lead to more oxygen vacancies to hydrate and fewer holes, rationalising the higher mass increase in wet N_2 than in wet air. No doubt, the high hydration or hydrogenation of the Fe-rich compounds interacts with the possibility for local restructuring and consequent oxidation, making the mass uptake appear irreversible.

Our conclusions are coherent with results from Zohourian et al. [1]. who showed that B-site Zn doping of barium and/or strontium ferrites enhances hydration and the explanation was that Zn reduces delocalization of holes from B-site cations to oxide ions. In further studies, Raimondi et al. [13]. employed various reduction and doping strategies to enhance proton concentration and used X-ray spectroscopy to analyse

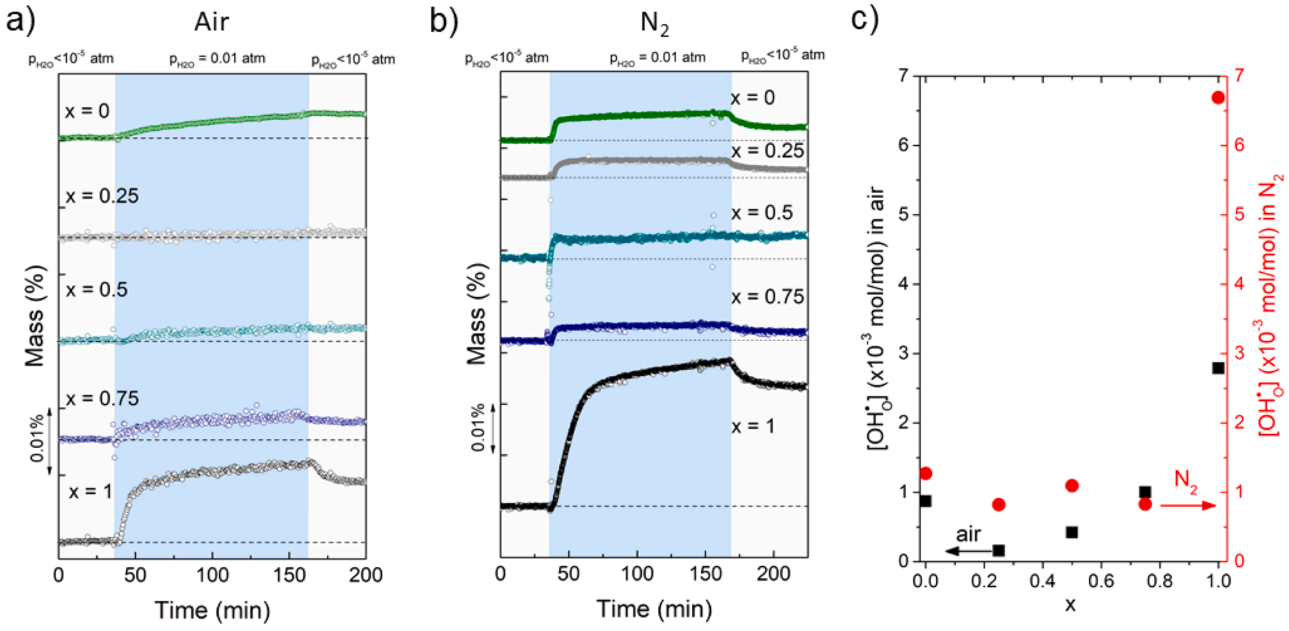

Fig. 7. Water uptake at 300 °C of $La_{0.5}Ba_{0.5}Co_{1-x}Fe_xO_{3-\delta}$ measured in air (a) and nitrogen (b) as well as estimated concentration of protonic defects (c).

how these strategies affect electronic states. The major conclusion was that the more localized holes are on B-site cations the better for hydration. All in all, large polaronic ligand holes increase the electronic conductivity, but at the expense of proton concentration and protonic conductivity.

3.7. *Surface hydration*

The flux of protons between the electrolyte and catalytic surface sites on the electrode may also go by dissociated water on the surface[37] . To evaluate the affinity of the surface to water and protons, a room temperature study of water sorption was performed, and the results for specimen with low and high iron content are depicted in Fig. 8a and b, respectively. One can see that the isotherm types are different for these two groups. All samples exhibit a type V isotherm, which has been observed for water adsorption on hydrophobic micro- and mesoporous adsorbents in the past [38]. However, caution should be made on characterizing materials as hydrophobic solely on this basis as it does not always have to be the case. In the case of LBCF50 and LBCF75 S-shaped isotherms were observed and the steep adsorption step at high relative humidity (p/p_0) which suggests surface heterogeneity and confined geometry effects [39]. Iron-rich samples revealed higher water adsorption, which at first sight can be assigned to the larger specific surface of these samples measured by the BET method (Table S2). Fig. 8c summarizes the total water adsorption capacity as the mass of water per unit surface area of the specimen and represents the maximum amount of water that can be stored at the surface. There is no obvious trend, but generally the capacity increases with the Fe content. The α parameter (Fig. 8d) is expressed as a chemical activity of water vapour (in this case the relative pressure) at which half of the total water capacity is reached. It is a normalized parameter ($0 < \alpha < 1$) expressing the hydrophobicity of a surface and reflects the properties of the first layers of water [40]. The results show that the surfaces of our materials are slightly hydrophobic independent of the iron content. Thus, the adsorbed water, especially the chemisorbed water which can exist even at high temperatures, should not be correlated to the results observed in thermogravimetric water uptake measurement. This means that the thermogravimetry at 300 °C truly represents bulk processes only. This is coherent with our previous study where the effect of surface water was also negligible in water uptake experiments for cobaltites[4].

4. Conclusions

All investigated compounds across the series $La_{0.5}Ba_{0.5}Co_{1-x}Fe_xO_{3-\delta}$ ($x = 0–1$) are cubic perovskites with unit cell parameters decreasing with increasing iron content *x*. The thermal expansion has a chemical component from oxygen loss by reduction at high temperatures. Both thermal and chemical expansion coefficients decrease with iron content, and the thermochemical expansion coefficient (TCEC) of BLF is as low as $11 \cdot 10^{-6}$ 1/K, approaching typical values of electrolytes used in electrochemical devices. In terms of defects, the materials behave as semiconducting $LaMO_3$ perovskites with small band gaps and 50 % Ba substitution acting as acceptors compensated by electron holes and oxygen vacancies depending on *T* and pO_2. The electrical properties are dominated by p-type electron hole conduction with high large polaron mobilities for the Co-rich compositions at low temperatures, tending towards lower small polaron mobilities with increasing Fe content. Conductivities decreasing with increasing temperature or decreasing pO_2 reflect the decreasing concentration of charge carriers as electron holes are replaced by oxygen vacancies by reduction. XAS results show that Co is in a high spin state, takes on the main part of the cation oxidation state changes, and have hole states in orbitals overlapping with the O 2p ligand states, which gives large polaronic behaviour, while the hole on Fe is more localised at the cation as a small and less mobile polarons. Hydration is more pronounced in inert than in oxidising atmospheres, as oxygen vacancies are easier to hydrate than electron holes, and it increases with Fe content, in line with the general finding that holes overlapping to the oxide ions repel protons. All in all, Fe-rich compositions benefit from lower TCEC and higher hydration and hence expected proton permeability, at the cost of lower electronic conductivity. The materials exhibit slightly hydrophobic surfaces at room temperature irrespective of Fe content, suggesting weak chemisorption of the first water layer that we may need for proton transport at the higher temperatures of positrodes for proton ceramics – a matter that warrants further investigation.

CRediT authorship contribution statement

Sebastian L Wachowski: Writing – original draft, Supervision, Resources, Project administration, Methodology, Investigation, Funding acquisition, Formal analysis, Data curation, Conceptualization. **Iga Szpunar:** Writing – original draft, Methodology, Investigation, Formal analysis. **Joanna Pośpiech:** Visualization, Methodology, Investigation, Formal analysis. **Daria Balcerzak:** Investigation. **Aleksandra Mielewczyk-Gryń:** Methodology, Investigation, Funding acquisition. **Małgorzata Nadolska:** Methodology, Investigation. **María Balaguer:** Methodology, Investigation. **José M. Serra:** Supervision, Funding acquisition, Project administration. **Einar Vøllestad:** Resources, Project administration, Funding acquisition. **Maria Gazda:** Writing – review & editing, Investigation. **Ragnar Strandbakke:** Writing – review &

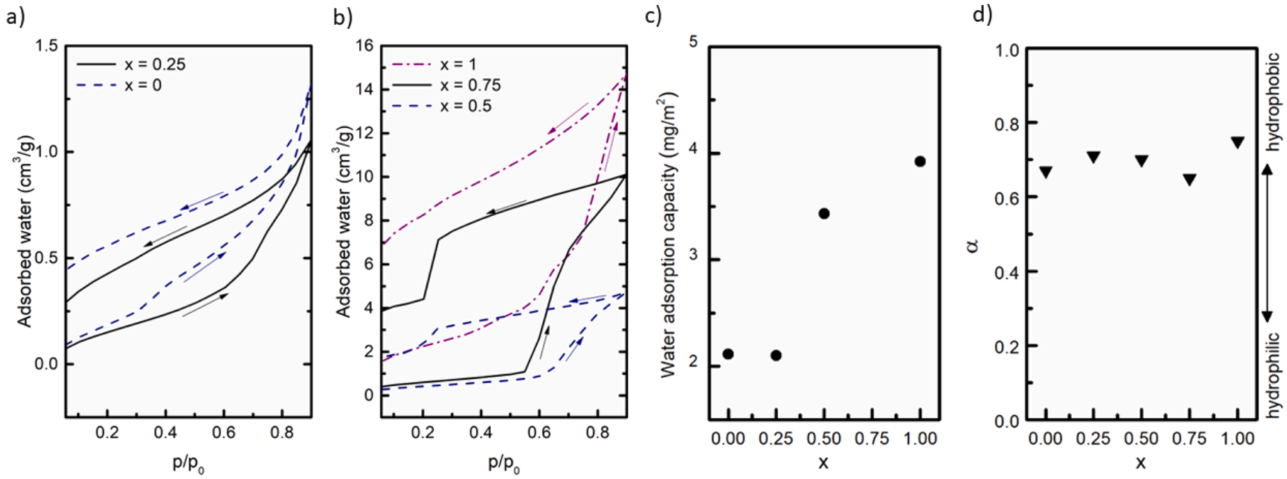

Fig. 8. Water sorption studies results: the isotherms are grouped for LBC, LBCF25 (a) and, LBCF50, LBCF75, LBF (b); while water adsorption capacity (c) and the α parameters (d) are plotted as a function of iron content x.

editing, Project administration, Funding acquisition. **Truls Norby:** Writing – review & editing, Supervision, Resources, Funding acquisition.

Declaration of competing interest

Acknowledgements

This work is financed by The Research Council of Norway (Grant n° 299736 "FunKeyCat") through the M-ERA.NET Joint Call 2018, and through project FunKeyCat supported by the National Science Centre, Poland under the M-ERA.NET 2, which has received funding from the European Union's Horizon 2020 research and innovation program under Grant agreement No 685451. Also M-ERA.NET in Spain and Spanish Ministry of Science and Innovation through the PCIN-2017–125, PIE 20238AT016, and RYC2021–033889-I funding is kindly acknowledged.

We acknowledge the Solaris National Radiation Centre Poland for access to the XAS/PEEM beamline (proposal ID 191011).

Supplementary materials

Supplementary material associated with this article can be found, in the online version, at doi:10.1016/j.actamat.2024.120585.

References

[1] R. Zohourian, R. Merkle, G. Raimondi, J. Maier, Mixed-conducting perovskites as cathode materials for protonic ceramic fuel cells: understanding the trends in proton uptake, Adv. Funct. Mater. 1801241 (2018) 1–10, https://doi.org/10.1002/adfm.201801241.

[2] E. Vøllestad, R. Strandbakke, M. Tarach, D. Catalán-Martínez, M.-L. Fontaine, D. Beeaff, D.R. Clark, J.M. Serra, T. Norby, Mixed proton and electron conducting double perovskite anodes for stable and efficient tubular proton ceramic electrolysers, Nat. Mater. 18 (2019) 752–759, https://doi.org/10.1038/s41563-019-0388-2.

[3] R. Pelosato, G. Cordaro, D. Stucchi, C. Cristiani, G. Dotelli, Cobalt based layered perovskites as cathode material for intermediate temperature solid oxide fuel cells: a brief review, J. Power Sources. 298 (2015) 46–67, https://doi.org/10.1016/j.jpowsour.2015.08.034.

[4] S.L. Wachowski, I. Szpunar, M.H. Sørby, A. Mielewczyk–Gryń, M. Balaguer, C. Ghica, M.C. Istrate, M. Gazda, A.E. Gunnæs, J.M. Serra, T. Norby, R. Strandbakke, Structure and water uptake in $BaLnCo_2O_{6-\delta}$ (Ln =La, Pr, Nd, Sm, Gd, Tb and Dy), Acta Mater. 199 (2020) 297–310, https://doi.org/10.1016/j.actamat.2020.08.018.

[5] E. Vøllestad, M. Schrade, J. Segalini, R. Strandbakke, T. Norby, Relating defect chemistry and electronic transport in the double perovskite $Ba_{1-x}Gd_{0.8}La_{0.2+x}Co_2O_{6-\delta}$ (BGLC), J. Mater. Chem. A. 5 (2017) 15743–15751, https://doi.org/10.1039/C7TA02659E.

[6] L. Zhao, J. Shen, B. He, F. Chen, C. Xia, Synthesis, characterization and evaluation of $PrBaCo_{2-x}Fe_xO_{5+\delta}$ as cathodes for intermediate-temperature solid oxide fuel cells, Int. J. Hydrogen Energy 36 (2011) 3658–3665, https://doi.org/10.1016/j.ijhydene.2010.12.064.

[7] J. Zhu, J.B. Gumundsdóttir, R. Strandbakke, K.G. Both, T. Aarholt, P.A. Carvalho, M.H. Sørby, I.J.T. Jensen, M.N. Guzik, T. Norby, H. Haug, A. Chatzitakis, Double perovskite cobaltites integrated in a monolithic and noble metal-free photoelectrochemical device for efficient water splitting, ACS Appl. Mater. Interfaces 13 (2021) 20313–20325, https://doi.org/10.1021/ACSAMI.1C01900/ASSET/IMAGES/MEDIUM/AM1C01900_M002.GIF.

[8] P. Wang, J. Yan, S. Wang, P. Xu, L. Shen, T. Song, Synergistic effects of lanthanum ferrite perovskite and hydrogen to promote ammonia production during microalgae catalytic pyrolysis process, Bioresour. Technol. 340 (2021) 125641, https://doi.org/10.1016/J.BIORTECH.2021.125641.

[9] O. Mihai, D. Chen, A. Holmen, Catalytic consequence of oxygen of lanthanum ferrite perovskite in chemical looping reforming of methane, Ind. Eng. Chem. Res. 50 (2011) 2613–2621, https://doi.org/10.1021/IE100651D/ASSET/IMAGES/LARGE/IE-2010-00651D_0010.JPEG.

[10] K.Y.A. Lin, Y.C. Chen, T.Y. Lin, H. Yang, Lanthanum cobaltite perovskite supported on zirconia as an efficient heterogeneous catalyst for activating Oxone in water, J. Colloid Interface Sci. 497 (2017) 325–332, https://doi.org/10.1016/J.JCIS.2017.03.004.

[11] N. Russo, S. Furfori, D. Fino, G. Saracco, V. Specchia, Lanthanum cobaltite catalysts for diesel soot combustion, Appl. Catal. B Environ. 83 (2008) 85–95, https://doi.org/10.1016/J.APCATB.2008.02.006.

[12] Y. Hisai, Q. Ma, T. Qureishy, T. Watanabe, T. Higo, T. Norby, Y. Sekine, Enhanced activity of catalysts on substrates with surface protonic current in an electrical field – a review, Chem. Commun. 57 (2021) 5737–5749, https://doi.org/10.1039/D1CC01551F.

[13] G. Raimondi, F. Giannici, A. Longo, R. Merkle, A. Chiara, M.F. Hoedl, A. Martorana, J. Maier, X-ray spectroscopy of $(Ba,Sr,La)(Fe,Zn,Y)O_{3-\delta}$ identifies structural and electronic features favoring proton uptake, Chem. Mater. 32 (2020) 8502–8511, https://doi.org/10.1021/acs.chemmater.0c02655.

[14] I. Szpunar, R. Strandbakke, M.H. Sørby, S.L. Wachowski, M. Balaguer, M. Tarach, J. M. Serra, A. Witkowska, E. Dzik, T. Norby, M. Gazda, A. Mielewczyk-Gryń, High-Temperature structural and electrical properties of $BaLnCo_2O_6$ positrodes, Materials 13 (2020) 4044, https://doi.org/10.3390/ma13184044.

[15] I. Szpunar, S. Wachowski, T. Miruszewski, K. Dzierzgowski, K. Górnicka, T. Klimczuk, M.H. Sørby, M. Balaguer, J.M. Serra, R. Strandbakke, M. Gazda, A. Mielewczyk-Gryń, Electric and magnetic properties of lanthanum barium cobaltite, J. Am. Ceram. Soc. 103 (2020) 1809–1818, https://doi.org/10.1111/jace.16865.

[16] R. Strandbakke, V.A. Cherepanov, A.Y. Zuev, D.S. Tsvetkov, C. Argirusis, G. Sourkouni, S. Prünte, T. Norby, Gd- and Pr-based double perovskite cobaltites as oxygen electrodes for proton ceramic fuel cells and electrolyser cells, Solid State Ionics 278 (2015) 120–132, https://doi.org/10.1016/j.ssi.2015.05.014.

[17] D. Gierszewska, I. Szpunar, F. Oseko, J. Pośpiech, M. Nadolska, M. Pieragowska, K. Reniecka, K. Waniek, K. Leszczyński, A. Mielewczyk-Gryń, M. Gazda, S. Wachowski, Microstructural design of $Ba_{0.5}La_{0.5}Co_{0.5}Fe_{0.5}O_3$ perovskite ceramics, Materials 14 (2021) 4656, https://doi.org/10.3390/ma14164656.

[18] A. Løken, S. Ricote, S. Wachowski, Thermal and chemical expansion in proton ceramic electrolytes and compatible electrodes, Crystals 8 (2018) 365, https://doi.org/10.3390/cryst8090365.

[19] C. Bernuy-Lopez, K. Høydalsvik, M.-A. Einarsrud, T. Grande, Effect of A-site cation ordering on chemical stability, oxygen stoichiometry and electrical conductivity in layered $LaBaCo_2O_{5+\delta}$ double perovskite, Materials (2016) 9, https://doi.org/10.3390/ma9030154.

[20] B. Kamecki, T. Miruszewski, K. Górnicka, T. Klimczuk, J. Karczewski, Characterization methods of nickel nano-particles obtained by the ex-solution process on the surface of Pr, Ni-doped $SrTiO_3$ perovskite ceramics, SN Appl. Sci. 1 (2019) 1–9, https://doi.org/10.1007/s42452-019-0317-7.

[21] A.A. Taskin, Y. Ando, Electron-hole asymmetry in $GdBaCo_2O_{5+x}$: evidence for spin blockade of electron transport in a correlated electron system, Phys. Rev. Lett. 95 (2005) 176603, https://doi.org/10.1103/PhysRevLett.95.176603.

[22] X. Zhang, X.-M. Wang, H.-W. Wei, X.-H. Lin, C.-H. Wang, Y. Zhang, C. Chen, X.-P. Jing, Effect of oxygen content on transport and magnetic properties of $PrBaCo_2O_{5.50+\delta}$, Mater. Res. Bull. 65 (2015) 80–88, https://doi.org/10.1016/J.MATERRESBULL.2015.01.021.

[23] C. Frontera, A. Caneiro, A.E. Carrillo, J. Oró-Solé, J.L. García-Muñoz, Tailoring oxygen content on $PrBaCo_2O_{5+\delta}$ layered cobaltites, Chem. Mater. 17 (2005) 5439–5445, https://doi.org/10.1021/cm051148q.

[24] T. Miruszewski, K. Dzierzgowski, P. Winiarz, D. Jaworski, K. Wiciak-Pawłowska, W. Skubida, S. Wachowski, A. Mielewczyk-Gryń, M. Gazda, Structure and transport properties of triple-conducting $Ba_xSr_{1-x}Ti_{1-y}Fe_yO_{3-\delta}$ oxides, RSC Adv. 11 (2021) 19570–19578, https://doi.org/10.1039/D0RA10048J.

[25] T. Miruszewski, W. Skubida, P. Winiarz, K. Dzierzgowski, A. Mielewczyk-Gryń, S. Wachowski, M. Gazda, Proton-Electron hole interactions in $Sr(Ti,Fe)O_{3-\delta}$ mixed-conducting perovskites, J. Electrochem. Soc. 169 (2022) 054522, https://doi.org/10.1149/1945-7111/AC6E8F.

[26] B.H. Toby, R.B. Von Dreele, GSAS-II: the genesis of a modern open-source all purpose crystallography software package, J. Appl. Crystallogr. 46 (2013) 544–549, https://doi.org/10.1107/S0021889813003531.

[27] T. Miruszewski, K. Dzierzgowski, P. Winiarz, S. Wachowski, A. Mielewczyk-Gryń, M. Gazda, Structural properties and water uptake of $SrTi_{1-x}Fe_xO_{3-x/2-\delta}$, Materials 13 (2020) 965, https://doi.org/10.3390/ma13040965.

[28] A.A. Taskin, A.N. Lavrov, Y. Ando, Achieving fast oxygen diffusion in perovskites by cation ordering, Appl. Phys. Lett. 86 (2005) 1–3, https://doi.org/10.1063/1.1864244.

[29] L. Wang, R. Merkle, J. Maier, T. Acartürk, U. Starke, Oxygen tracer diffusion in dense $Ba_{0.5}Sr_{0.5}Co_{0.8}Fe_{0.2}O_{3-\delta}$ films, Appl. Phys. Lett. 94 (2009) 071908, https://doi.org/10.1063/1.3085969.

[30] D.A. Malyshkin, A.Y. Novikov, D.S. Tsvetkov, Oxygen content and defect structure of the perovskite $La_{0.5}Ba_{0.5}CoO_{3-\delta}$, Chim. Techno Acta 5 (2018) 117–124, https://doi.org/10.15826/chimtech.2018.5.4.04.

[31] A.J. Bosman, H.J. van Daal, Small-polaron versus band conduction in some transition-metal oxides, Adv. Phys. 19 (1970) 1–117, https://doi.org/10.1080/00018737000101071.

[32] A. Maignan, V. Caignaert, B. Raveau, D. Khomskii, G. Sawatzky, Thermoelectric power of $HoBaCo_2O_{5.5}$: possible evidence of the spin blockade in cobaltites, Phys. Rev. Lett. 93 (2004) 026–401, https://doi.org/10.1103/PhysRevLett.93.026401.

[33] K. Conder, E. Pomjakushina, V. Pomjakushin, M. Stingaciu, S. Streule, A. Podlesnyak, Oxygen isotope effect on metal-insulator transition in layered cobaltites $RBaCo_2O_{5.5}$ (R = Pr, Dy, Ho and Y), J. Phys. Condens. Matter. 17 (2005) 5813–5820, https://doi.org/10.1088/0953-8984/17/37/016.

[34] D. Guan, J. Zhou, Z. Hu, W. Zhou, X. Xu, Y. Zhong, B. Liu, Y. Chen, M. Xu, H.J. Lin, C. Te Chen, J.Q. Wang, Z. Shao, Searching general sufficient-and-necessary conditions for ultrafast hydrogen-evolving electrocatalysis, Adv. Funct. Mater. (2019) 29, https://doi.org/10.1002/adfm.201900704.

[35] A.S. Harvey, Z. Yang, A. Infortuna, D. Beckel, J.A. Purton, L.J. Gauckler, Development of electron holes across the temperature-induced semiconductor–metal transition in $Ba_{1-x}Sr_xCo_{1-y}Fe_yO_{3-\delta}$ (x, y =

0.2–0.8): a soft x-ray absorption spectroscopy study, J. Phys. Condens. Matter. 21 (2009) 015801, https://doi.org/10.1088/0953-8984/21/1/015801.

[36] Z. Hu, H. Wu, M.W. Haverkort, H.H. Hsieh, H.-J. Lin, T. Lorenz, J. Baier, A. Reichl, I. Bonn, C. Felser, A. Tanaka, C.T. Chen, L.H. Tjeng, Different look at the spin state of Co3+ ions in a CoO5 pyramidal coordination, Phys. Rev. Lett. 92 (2004) 207402, https://doi.org/10.1103/PhysRevLett.92.207402.

[37] T. Norby, Protonic conduction on oxide surfaces—Role and applications in electrochemical energy conversion, Prog. Energy 6 (2024) 043002, https://doi.org/10.1088/2516-1083/ad6c9f.

[38] C. Schlumberger, M. Thommes, Characterization of hierarchically ordered porous materials by physisorption and mercury porosimetry—a tutorial review, Adv. Mater. Interfaces 8 (2021) 2002181, https://doi.org/10.1002/admi.202002181.

[39] L.F. Velasco, R. Guillet-Nicolas, G. Dobos, M. Thommes, P. Lodewyckx, Towards a better understanding of water adsorption hysteresis in activated carbons by scanning isotherms, Carbon 96 (2016) 753–758, https://doi.org/10.1016/j.carbon.2015.10.017.

[40] J. Canivet, A. Fateeva, Y. Guo, B. Coasne, D. Farrusseng, Water adsorption in MOFs: fundamentals and applications, Chem. Soc. Rev. 43 (2014) 5594–5617, https://doi.org/10.1039/C4CS00078A.